Commun. Comput. Phys.
doi: 10.4208/cicp.030710.131210s

Vol. **11**, No. 4, pp. 1144-1168
April 2012

Improvement on Spherical Symmetry in Two-Dimensional Cylindrical Coordinates for a Class of Control Volume Lagrangian Schemes

Juan Cheng[1] and Chi-Wang Shu[2,*]

[1] *Laboratory of Computational Physics, Institute of Applied Physics and Computational Mathematics, Beijing 100088, China.*
[2] *Division of Applied Mathematics, Brown University, Providence, RI 02912, USA.*

Received 3 July 2010; Accepted (in revised version) 13 December 2010

Available online 29 November 2011

Abstract. In [14], Maire developed a class of cell-centered Lagrangian schemes for solving Euler equations of compressible gas dynamics in cylindrical coordinates. These schemes use a node-based discretization of the numerical fluxes. The control volume version has several distinguished properties, including the conservation of mass, momentum and total energy and compatibility with the geometric conservation law (GCL). However it also has a limitation in that it cannot preserve spherical symmetry for one-dimensional spherical flow. An alternative is also given to use the first order area-weighted approach which can ensure spherical symmetry, at the price of sacrificing conservation of momentum. In this paper, we apply the methodology proposed in our recent work [8] to the first order control volume scheme of Maire in [14] to obtain the spherical symmetry property. The modified scheme can preserve one-dimensional spherical symmetry in a two-dimensional cylindrical geometry when computed on an equal-angle-zoned initial grid, and meanwhile it maintains its original good properties such as conservation and GCL. Several two-dimensional numerical examples in cylindrical coordinates are presented to demonstrate the good performance of the scheme in terms of symmetry, non-oscillation and robustness properties.

AMS subject classifications: 65M06, 76M20

Key words: Control volume Lagrangian scheme, spherical symmetry preservation, conservative, cell-centered, compressible flow, cylindrical coordinates.

1 Introduction

The Lagrangian method is one of the main numerical methods for simulating multidimensional fluid flow, in which the mesh moves with the local fluid velocity. It is widely

*Corresponding author. *Email addresses:* cheng_juan@iapcm.ac.cn (J. Cheng), shu@dam.brown.edu (C.-W. Shu)

used in many fields for multi-material flow simulations such as astrophysics, inertial confinement fusion (ICF) and computational fluid dynamics (CFD), due to its distinguished advantage in capturing material interfaces automatically and sharply. There are two kinds of Lagrangian methods. One is built on a staggered discretization in which velocity (momentum) is stored at vertices, while density and internal energy are stored at cell centers. The density/internal energy and velocity are solved on two different control volumes, see, e.g., [1, 3, 18]. This kind of Lagrangian schemes usually uses an artificial viscosity term, for example [4,5,18], to ensure the dissipation of kinetic energy into internal energy through shock waves. The other is based on the cell-centered discretization in which density, momentum and total energy are all centered within cells and evolved on the same control volume, e.g., [6,7,10,13,15,17]. This kind of schemes does not require the addition of an explicit artificial viscosity for shock capturing. Numerical diffusion is implicitly contained in the Riemann solvers.

It is a critical issue for a Lagrangian scheme to keep certain symmetry in a coordinate system different from that symmetry. For example, in the simulation of implosions, since the small deviation from spherical symmetry due to numerical errors may be amplified by Rayleigh-Taylor or other instabilities which may lead to unexpected large errors, it is very important for the scheme to keep the spherical symmetry. In the past several decades, many research works have been performed concerning the spherical symmetry preservation in two-dimensional cylindrical coordinates. The most widely used method that keeps spherical symmetry exactly on an equal-angle-zoned grid in cylindrical coordinates is the area-weighted method [2, 3, 14, 20, 22, 23]. In this approach one uses a Cartesian form of the momentum equation in the cylindrical coordinate system, hence integration is performed on area rather than on the true volume in cylindrical coordinates. However, these area-weighted schemes have a flaw in that they may violate momentum conservation. Margolin and Shashkov used a curvilinear grid to construct symmetry-preserving discretizations for Lagrangian gas dynamics [16]. In our recent work [8], we have developed a new cell-centered control volume Lagrangian scheme for solving Euler equations of compressible gas dynamics in two-dimensional cylindrical coordinates. Based on the strategy of local coordinate transform and a careful treatment of the source term in the momentum equation, the scheme is designed to be able to preserve one-dimensional spherical symmetry in a two-dimensional cylindrical geometry when computed on an equal-angle-zoned initial grid. A distinguished feature of our scheme is that it can keep both the symmetry and conservation properties on the straight-line grid. However, our scheme in [8] does not satisfy the geometric conservation law (GCL).

In [14], Maire developed a class of high order cell-centered Lagrangian schemes for solving Euler equations of compressible gas dynamics in cylindrical coordinates. A node-based discretization of the numerical fluxes is given which makes the finite volume scheme compatible with the geometric conservation law. Both the control volume and area-weighted discretizations of the momentum equations are presented in [14]. The control volume scheme is conservative for mass, momentum and total energy, and satisfies a local entropy inequality in its first-order semi-discrete form. However, it does not

preserve spherical symmetry. On the other hand, the first order area-weighted scheme is conservative for mass and total energy and preserves spherical symmetry for one-dimensional spherical flow on equal-angle polar grid, but it cannot preserve the momentum conservation and does not satisfy the entropy inequality. Numerical tests are given in [14] which verify the robustness of the schemes.

In this paper, we attempt to apply the strategy proposed in [8] on Maire's first order control volume Lagrangian scheme [14] to improve its property in symmetry preservation while keeping its main original good properties including GCL, conservation of mass, momentum and total energy.

An outline of the rest of this paper is as follows. In Section 2, we describe the modified scheme and discuss some critical issues such as GCL, conservation and spherical symmetry preservation about the scheme. In Section 3, numerical examples are given to demonstrate the performance of the new modified cell-centered Lagrangian scheme. In Section 4 we will give concluding remarks.

2 The improvement on the cell-centered control volume Lagrangian scheme of Maire in cylindrical coordinates

2.1 The compressible Euler equations in a Lagrangian formulation in cylindrical coordinates

The compressible inviscid flow is governed by the Euler equations which have the following integral form in the Lagrangian formulation

$$\begin{cases} \dfrac{\mathrm{d}}{\mathrm{d}t}\iint_{\Omega(t)}\rho \mathrm{d}V=0, \\ \dfrac{\mathrm{d}}{\mathrm{d}t}\iint_{\Omega(t)}\rho\mathbf{u}\mathrm{d}V=-\int_{\Gamma(t)}P\mathbf{n}\mathrm{d}s, \\ \dfrac{\mathrm{d}}{\mathrm{d}t}\iint_{\Omega(t)}\rho E\mathrm{d}V=-\int_{\Gamma(t)}P\mathbf{u}\cdot\mathbf{n}\mathrm{d}s, \end{cases} \tag{2.1}$$

where ρ is the density, P is the pressure, $\mathbf{u}$ is the vector of velocity, E is the specific total energy, and $\mathbf{n}$ is the unit outward normal to the boundary $\Gamma(t)$.

The geometric conservation law refers to the fact that the rate of change of a Lagrangian volume should be computed consistently with the node motion, which can be formulated as

$$\frac{\mathrm{d}}{\mathrm{d}t}\iint_{\Omega(t)}\mathrm{d}V=\int_{\Gamma(t)}\mathbf{u}\cdot\mathbf{n}\mathrm{d}s. \tag{2.2}$$

In this paper, we seek to study the axisymmetric compressible Euler system. Its specific

form in the cylindrical coordinates is as follows

$$\begin{cases} \dfrac{\mathrm{d}}{\mathrm{d}t}\iint_{\Omega(t)}\rho r\mathrm{d}r\mathrm{d}z=0, \\ \dfrac{\mathrm{d}}{\mathrm{d}t}\iint_{\Omega(t)} r\mathrm{d}r\mathrm{d}z=\int_{\Gamma(t)}\mathbf{u}\cdot\mathbf{n}r\mathrm{d}l, \\ \dfrac{\mathrm{d}}{\mathrm{d}t}\iint_{\Omega(t)}\rho u_z r\mathrm{d}r\mathrm{d}z=-\int_{\Gamma(t)}Pn_z r\mathrm{d}l, \\ \dfrac{\mathrm{d}}{\mathrm{d}t}\iint_{\Omega(t)}\rho u_r r\mathrm{d}r\mathrm{d}z=-\int_{\Gamma(t)}Pn_r r\mathrm{d}l+\iint_{\Omega(t)}P\mathrm{d}r\mathrm{d}z, \\ \dfrac{\mathrm{d}}{\mathrm{d}t}\iint_{\Omega(t)}\rho E r\mathrm{d}r\mathrm{d}z=-\int_{\Gamma(t)}P\mathbf{u}\cdot\mathbf{n}r\mathrm{d}l, \end{cases} \tag{2.3}$$

where z and r are the axial and radial directions respectively. $\mathbf{u}=(u_z,u_r)$, where u_z, u_r are the velocity components in the z and r directions respectively, and $\mathbf{n}=(n_z,n_r)$ is the unit outward normal to the boundary $\Gamma(t)$ in the z-r coordinates.

The set of equations is completed by the addition of an equation of state (EOS) with the following general form

$$P=P(\rho,e), \tag{2.4}$$

where $e=E-|\mathbf{u}|^2/2$ is the specific internal energy. Especially, if we consider the ideal gas, then the equation of state has a simpler form

$$P=(\gamma-1)\rho e,$$

where γ is a constant representing the ratio of specific heat capacities of the fluid.

In the next subsection, we will first summarize the control volume scheme of Maire in [14].

2.2 The control volume scheme of Maire in cylindrical coordinates

2.2.1 Notations and assumptions

We will mostly use the notations in [14]. The 2D spatial domain Ω is discretized into quadrangular computational cells. Each quadrangular cell is assigned a unique index c, and is denoted by $\Omega_c(t)$. The boundary of the cell Ω_c is denoted as $\partial\Omega_c$. Each vertex of the mesh is assigned a unique index p and we denote the counterclockwise ordered list of the vertices of the cell Ω_c by $p(c)$. The cell Ω_c is surrounded by four cells denoted as Ω_b, Ω_r, Ω_t, Ω_l which correspond to the bottom, right, top and left positions respectively. A_c denotes the area of the cell Ω_c. V_c is the volume of the cell, that is, the volume of the circular ring obtained by rotating this cell around the azimuthal z-axis (without the 2π factor).

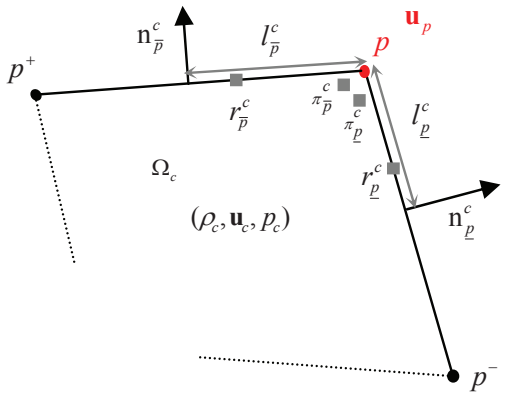

Figure 1: Notations related to the cell Ω_c.

Using these notations, the set of Eq. (2.3) can be rewritten in the following control volume formulation

$$m_c \frac{\mathrm{d}}{\mathrm{d}t}\left(\frac{1}{\rho_c}\right) = \int_{\partial\Omega_c} \mathbf{u}\cdot\mathbf{n} r \mathrm{d}l, \qquad m_c \frac{\mathrm{d}}{\mathrm{d}t} u_c^z = -\int_{\partial\Omega_c} P n_z r \mathrm{d}l, \tag{2.5a}$$

$$m_c \frac{\mathrm{d}}{\mathrm{d}t} u_c^r = -\int_{\partial\Omega_c} P n_r r \mathrm{d}l + \iint_{\Omega_c} P \mathrm{d}r\mathrm{d}z, \qquad m_c \frac{\mathrm{d}}{\mathrm{d}t} E_c = -\int_{\partial\Omega_c} P\mathbf{u}\cdot\mathbf{n} r \mathrm{d}l, \tag{2.5b}$$

where $m_c = \iint_{\Omega_c} \rho r \mathrm{d}r\mathrm{d}z$ denotes the mass in the cell Ω_c, which keeps constant during the time marching according to the first equation in (2.3). ρ_c, $\mathbf{u}_c = (u_c^z, u_c^r)$ and E_c represent the density, velocity and total energy of the cell Ω_c which are defined as follows

$$\rho_c = \frac{1}{V_c}\iint_{\Omega_c} \rho r \mathrm{d}r\mathrm{d}z, \qquad u_c^z = \frac{1}{m_c}\iint_{\Omega_c} \rho u_z r \mathrm{d}r\mathrm{d}z,$$

$$u_c^r = \frac{1}{m_c}\iint_{\Omega_c} \rho u_r r \mathrm{d}r\mathrm{d}z, \qquad E_c = \frac{1}{m_c}\iint_{\Omega_c} \rho E r \mathrm{d}r\mathrm{d}z.$$

The coordinates and velocity of the point p are denoted as (z_p, r_p) and $\mathbf{u}_p = (u_p^z, u_p^r)$ respectively. l_{pp^-} and l_{pp^+} denote the lengths of the edges $[p^-, p]$ and $[p, p^+]$, and $\mathbf{n}_{pp^-}$ and $\mathbf{n}_{pp^+}$ are the corresponding unit outward normals, where p^-, p^+ are the two neighboring points of the point p (see Fig. 1).

In the cell-centered control volume Lagrangian scheme presented in [14], the discrete gradient operators over the cell Ω_c are constructed by introducing two nodal pressures at each node p of the cell Ω_c. These pressures are denoted as $\pi^c_{\underline{p}}$ and $\pi^c_{\bar{p}}$, see Fig. 1. They are related to the two edges sharing the node p. The half lengths and the unit outward normals of the edges connected to the point p are denoted as follows

$$l^c_{\underline{p}} = \frac{1}{2} l_{pp^-}, \qquad l^c_{\bar{p}} = \frac{1}{2} l_{pp^+}, \qquad \mathbf{n}^c_{\underline{p}} = \mathbf{n}_{pp^-}, \qquad \mathbf{n}^c_{\bar{p}} = \mathbf{n}_{pp^+}. \tag{2.6}$$

The pseudo radii $r^c_{\underline{p}}$ and $r^c_{\overline{p}}$ are defined as

$$r^c_{\underline{p}}=\frac{1}{3}(2r_p+r_{p^-}),\qquad r^c_{\overline{p}}=\frac{1}{3}(2r_p+r_{p^+}). \tag{2.7}$$

2.2.2 Computation of nodal velocity and pressure

In the paper [14], the specific way in determining the nodal velocity and pressure guarantees that the scheme satisfies the following sufficient condition for total energy conservation

$$\sum_{c\in c(p)}(r^c_{\underline{p}}l^c_{\underline{p}}\pi^c_{\underline{p}}n^{c,r}_{\underline{p}}+r^c_{\overline{p}}l^c_{\overline{p}}\pi^c_{\overline{p}}n^{c,r}_{\overline{p}})=0, \tag{2.8}$$

where $c(p)$ is the set of the cells around the point p.

The specific formulas to calculate the nodal velocity $\mathbf{u}_p$ and nodal pressures $\pi^c_{\underline{p}}$ and $\pi^c_{\overline{p}}$ are as follows

$$\mathbf{u}_p=M_p^{-1}\sum_{c\in c(p)}\left(r^c_{\underline{p}}l^c_{\underline{p}}\mathbf{n}^c_{\underline{p}}+r^c_{\overline{p}}l^c_{\overline{p}}\mathbf{n}^c_{\overline{p}}\right)P_c+\mathbf{u}_c, \tag{2.9a}$$

$$P_c-\pi^c_{\underline{p}}=z^c_{\underline{p}}(\mathbf{u}_p-\mathbf{u}_c)\cdot\mathbf{n}^c_{\underline{p}},\qquad P_c-\pi^c_{\overline{p}}=z^c_{\overline{p}}(\mathbf{u}_p-\mathbf{u}_c)\cdot\mathbf{n}^c_{\overline{p}}, \tag{2.9b}$$

where P_c is the pressure of the cell Ω_c determined by $\{\rho_c,\mathbf{u}_c,E_c\}$. The 2×2 matrices M_{pc} and M_p are denoted as

$$M_{pc}=z^c_{\underline{p}}r^c_{\underline{p}}l^c_{\underline{p}}\left(\mathbf{n}^c_{\underline{p}}\otimes\mathbf{n}^c_{\underline{p}}\right)+z^c_{\overline{p}}r^c_{\overline{p}}l^c_{\overline{p}}\left(\mathbf{n}^c_{\overline{p}}\otimes\mathbf{n}^c_{\overline{p}}\right),\qquad M_p=\sum_{c\in c(p)}M_{pc}, \tag{2.10}$$

where $z^c_{\underline{p}}$ and $z^c_{\overline{p}}$ are the mass fluxes swept by the waves which can be determined in several ways, such as the Dukowicz approach or the acoustic approach. We refer the reader to the paper [14] for more details. In this paper, we will only use the acoustic approach, that is

$$z^c_{\underline{p}}=z^c_{\overline{p}}=\rho_c a_c, \tag{2.11}$$

where a_c is the local isentropic speed of sound.

After we get the nodal velocity $\mathbf{u}_p$ at the point p, the point moves with the following local kinematic equation

$$\frac{\mathrm{d}}{\mathrm{d}t}\mathbf{x}_p=\mathbf{u}_p,\qquad \mathbf{x}_p(0)=\mathbf{x}^0_p, \tag{2.12}$$

where $\mathbf{x}_p=(z_p,r_p)$ defines the position of the point p at $t>0$ and $\mathbf{x}^0_p$ denotes its initial position.

2.2.3 Spatial discretization

The semi-discrete finite volume scheme of the governing equations (2.5) is of the following form

$$m_c\frac{\mathrm{d}}{\mathrm{d}t}\left(\frac{1}{\rho_c}\right)-\sum_{p\in p(c)}\left(r^c_{\underline{p}}l^c_{\underline{p}}\mathbf{n}^c_{\underline{p}}+r^c_{\overline{p}}l^c_{\overline{p}}\mathbf{n}^c_{\overline{p}}\right)\cdot\mathbf{u}_p=0, \tag{2.13a}$$

$$m_c\frac{\mathrm{d}}{\mathrm{d}t}u^z_c+\sum_{p\in p(c)}\left(r^c_{\underline{p}}l^c_{\underline{p}}\pi^c_{\underline{p}}n^{c,z}_{\underline{p}}+r^c_{\overline{p}}l^c_{\overline{p}}\pi^c_{\overline{p}}n^{c,z}_{\overline{p}}\right)=0, \tag{2.13b}$$

$$m_c\frac{\mathrm{d}}{\mathrm{d}t}u^r_c+\sum_{p\in p(c)}\left(r^c_{\underline{p}}l^c_{\underline{p}}\pi^c_{\underline{p}}n^{c,r}_{\underline{p}}+r^c_{\overline{p}}l^c_{\overline{p}}\pi^c_{\overline{p}}n^{c,r}_{\overline{p}}\right)-A_cP_c=0, \tag{2.13c}$$

$$m_c\frac{\mathrm{d}}{\mathrm{d}t}E_c+\sum_{p\in p(c)}\left(r^c_{\underline{p}}l^c_{\underline{p}}\pi^c_{\underline{p}}\mathbf{n}^c_{\underline{p}}+r^c_{\overline{p}}l^c_{\overline{p}}\pi^c_{\overline{p}}\mathbf{n}^c_{\overline{p}}\right)\cdot\mathbf{u}_p=0, \tag{2.13d}$$

where $n^{c,z}_{\underline{p}}$,$n^{c,z}_{\overline{p}}$ and $n^{c,r}_{\underline{p}}$,$n^{c,r}_{\overline{p}}$ are the components of $\mathbf{n}^c_{\underline{p}}$ and $\mathbf{n}^c_{\overline{p}}$ along the z and r directions respectively.

2.2.4 Time discretization

The time discretization for the equation of nodal movement (2.12) is the Euler forward method given as follows

$$z^{n+1}_p=z^n_p+\Delta t^n u^{z,n}_p,\qquad r^{n+1}_p=r^n_p+\Delta t^n u^{r,n}_p, \tag{2.14}$$

where $u^{z,n}_p$,$u^{r,n}_p$ are the z and r components of $\mathbf{u}_p$ at the nth time step.

As a first order scheme, the time marching for the semi-discrete scheme (2.5) can also be accomplished by the Euler forward method. Thus the fully discretized scheme can be written as follows

$$m_c\begin{pmatrix}\frac{1}{\rho^{n+1}_c}-\frac{1}{\rho^n_c}\\ u^{z,n+1}_c-u^{z,n}_c\\ u^{r,n+1}_c-u^{r,n}_c\\ E^{n+1}_c-E^n_c\end{pmatrix}=\Delta t^n\left(-\begin{pmatrix}-\sum_{p\in p(c)}\left(r^{c,n}_{\underline{p}}l^{c,n}_{\underline{p}}\mathbf{n}^{c,n}_{\underline{p}}+r^{c,n}_{\overline{p}}l^{c,n}_{\overline{p}}\mathbf{n}^{c,n}_{\overline{p}}\right)\cdot\mathbf{u}^n_p\\ \sum_{p\in p(c)}\left(r^{c,n}_{\underline{p}}l^{c,n}_{\underline{p}}\pi^{c,n}_{\underline{p}}n^{c,z,n}_{\underline{p}}+r^{c,n}_{\overline{p}}l^{c,n}_{\overline{p}}\pi^{c,n}_{\overline{p}}n^{c,z,n}_{\overline{p}}\right)\\ \sum_{p\in p(c)}\left(r^{c,n}_{\underline{p}}l^{c,n}_{\underline{p}}\pi^{c,n}_{\underline{p}}n^{c,r,n}_{\underline{p}}+r^{c,n}_{\overline{p}}l^{c,n}_{\overline{p}}\pi^{c,n}_{\overline{p}}n^{c,r,n}_{\overline{p}}\right)\\ \sum_{p\in p(c)}\left(r^{c,n}_{\underline{p}}l^{c,n}_{\underline{p}}\pi^{c,n}_{\underline{p}}\mathbf{n}^{c,n}_{\underline{p}}+r^{c,n}_{\overline{p}}l^{c,n}_{\overline{p}}\pi^{c,n}_{\overline{p}}\mathbf{n}^{c,n}_{\overline{p}}\right)\cdot\mathbf{u}^n_p\end{pmatrix}+\begin{pmatrix}0\\0\\A^n_cP^n_c\\0\end{pmatrix}\right). \tag{2.15}$$

Here the variables with the superscripts n and $n+1$ represent the values of the corresponding variables at the nth and $(n+1)$th time steps respectively. The scheme (2.15) is consistent with the Euler equations (2.5) and has first order accuracy in space and time.

In [14], the time step Δt^n is controlled by both the CFL condition and the criterion on the variation of volume, that is, the CFL condition is satisfied as follows

$$\Delta t_e = C_e \min_c \left(\frac{l_c^n}{a_c^n} \right),$$

where l_c^n is the shortest edge length of the cell Ω_c, and a_c^n is the sound speed within this cell. C_e is the Courant number which is set to be 0.5 unless otherwise stated in the following tests.

The criterion on the variation of volume is accomplished as

$$\Delta t_v = C_v \left\{ V_c^n \left| \frac{d}{dt} V_c(t^n) \right|^{-1} \right\},$$

where

$$\frac{d}{dt} V_c(t^n) = \frac{V_c^{n+1} - V_c^n}{\Delta t^n}.$$

The parameter $C_v = 0.1$ is used in the numerical simulations.

Finally, the next time step Δt^{n+1} is given by

$$\Delta t^{n+1} = \min \left(\Delta t_e, \Delta t_v, C_m \Delta t^n \right),$$

where $C_m = 1.01$.

2.3 The improvement of the scheme on the symmetry property

The control volume scheme (2.15) is theoretically proven to have many good properties such as the conservation, GCL and entropy inequality, and is also verified to have good performance in practical simulations. However, it has a limitation in not being able to preserve the spherical symmetry. In this paper, we attempt to improve the scheme in this aspect using the strategy of our recent work [8]. Somewhat differently from the approach of the explicit local coordinate transform in [8], here we perform the improvement on the scheme (2.13) in z-r coordinates directly and use local coordinate transform only in the symmetry-preserving proof but not in the actual implementation of the algorithm. In fact, the key ingredient to make the scheme satisfy the spherical symmetry property in a 2D cylindrical geometry is the treatment of the source term. To be more specific, we replace P_c in the source term of the r-momentum equation in (2.13) by P_a which is defined as follows

$$P_a = \frac{1}{4} \left(\pi_{\underline{1}}^c + \pi_{\underline{2}}^c + \pi_{\underline{3}}^c + \pi_{\underline{4}}^c \right), \tag{2.16}$$

where $\pi_{\underline{1}}^c$, $\pi_{\underline{2}}^c$, $\pi_{\underline{3}}^c$ and $\pi_{\underline{4}}^c$ are the values of pressure related to the two radial edges of the cell Ω_c (see Fig. 2). We can easily see that $A_c P_a$ approximates $\iint_{\Omega_c} P dr dz$ with the same order as $A_c P_c$.

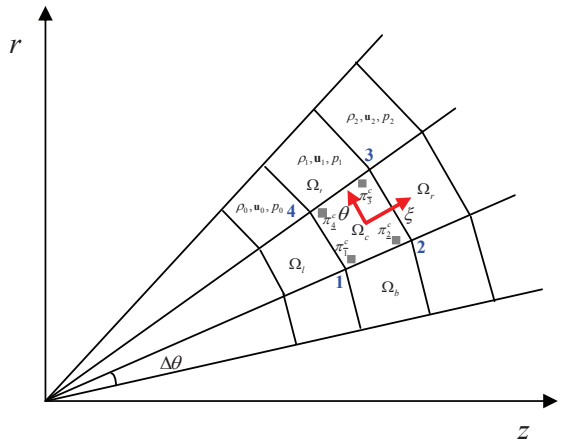

Figure 2: Equi-angular polar grid for the cylindrical geometry.

Thus, the difference between the modified scheme and the original scheme lies only in the expression of the r-momentum equation. In summary, the modified semi-discrete scheme can be expressed as follows

$$m_c \frac{\mathrm{d}}{\mathrm{d}t}\left(\frac{1}{\rho_c}\right) - \sum_{p\in p(c)} \left(r_{\underline{p}}^c l_{\underline{p}}^c \mathbf{n}_{\underline{p}}^c + r_{\overline{p}}^c l_{\overline{p}}^c \mathbf{n}_{\overline{p}}^c\right)\cdot \mathbf{u}_p = 0, \tag{2.17a}$$

$$m_c \frac{\mathrm{d}}{\mathrm{d}t} u_c^z + \sum_{p\in p(c)} \left(r_{\underline{p}}^c l_{\underline{p}}^c \pi_{\underline{p}}^c n_{\underline{p}}^{c,z} + r_{\overline{p}}^c l_{\overline{p}}^c \pi_{\overline{p}}^c n_{\overline{p}}^{c,z}\right) = 0, \tag{2.17b}$$

$$m_c \frac{\mathrm{d}}{\mathrm{d}t} u_c^r + \sum_{p\in p(c)} \left(r_{\underline{p}}^c l_{\underline{p}}^c \pi_{\underline{p}}^c n_{\underline{p}}^{c,r} + r_{\overline{p}}^c l_{\overline{p}}^c \pi_{\overline{p}}^c n_{\overline{p}}^{c,r}\right) - A_c P_a = 0, \tag{2.17c}$$

$$m_c \frac{\mathrm{d}}{\mathrm{d}t} E_c + \sum_{p\in p(c)} \left(r_{\underline{p}}^c l_{\underline{p}}^c \pi_{\underline{p}}^c \mathbf{n}_{\underline{p}}^c + r_{\overline{p}}^c l_{\overline{p}}^c \pi_{\overline{p}}^c \mathbf{n}_{\overline{p}}^c\right)\cdot \mathbf{u}_p = 0. \tag{2.17d}$$

The fully discretized modified scheme is of the following expression

$$m_c \begin{pmatrix} \frac{1}{\rho_c^{n+1}} - \frac{1}{\rho_c^n} \\ u_c^{z,n+1} - u_c^{z,n} \\ u_c^{r,n+1} - u_c^{r,n} \\ E_c^{n+1} - E_c^n \end{pmatrix} = \Delta t^n \left(- \begin{pmatrix} -\sum_{p\in p(c)} \left(r_{\underline{p}}^{c,n} l_{\underline{p}}^{c,n} \mathbf{n}_{\underline{p}}^{c,n} + r_{\overline{p}}^{c,n} l_{\overline{p}}^{c,n} \mathbf{n}_{\overline{p}}^{c,n}\right)\cdot \mathbf{u}_p^n \\ \sum_{p\in p(c)} \left(r_{\underline{p}}^{c,n} l_{\underline{p}}^{c,n} \pi_{\underline{p}}^{c,n} n_{\underline{p}}^{c,z,n} + r_{\overline{p}}^{c,n} l_{\overline{p}}^{c,n} \pi_{\overline{p}}^{c,n} n_{\overline{p}}^{c,z,n}\right) \\ \sum_{p\in p(c)} \left(r_{\underline{p}}^{c,n} l_{\underline{p}}^{c,n} \pi_{\underline{p}}^{c,n} n_{\underline{p}}^{c,r,n} + r_{\overline{p}}^{c,n} l_{\overline{p}}^{c,n} \pi_{\overline{p}}^{c,n} n_{\overline{p}}^{c,r,n}\right) \\ \sum_{p\in p(c)} \left(r_{\underline{p}}^{c,n} l_{\underline{p}}^{c,n} \pi_{\underline{p}}^{c,n} \mathbf{n}_{\underline{p}}^{c,n} + r_{\overline{p}}^{c,n} l_{\overline{p}}^{c,n} \pi_{\overline{p}}^{c,n} \mathbf{n}_{\overline{p}}^{c,n}\right)\cdot \mathbf{u}_p^n \end{pmatrix} + \begin{pmatrix} 0 \\ 0 \\ A_c^n P_a^n \\ 0 \end{pmatrix} \right). \tag{2.18}$$

2.3.1 The issue of conservation, GCL and entropy inequality

Compared with the scheme (2.15) of Maire [14], we only use an alternative approach (2.16) to the pressure appearing in the source term of the r-momentum equation to guarantee the scheme's spherical symmetry preservation property that will be shown in the following section. Since we do not make any change on any other terms in the original scheme (2.15), the modified scheme (2.18) can also satisfy the conservation for the mass, z-momentum and total energy just as the original scheme. As to the conservation of the r-momentum, summing the r-momentum equation in (2.17) over all the cells, we have

$$\frac{\mathrm{d}}{\mathrm{d}t}\Big(\sum_c m_c u_c^r\Big) = -\sum_c \Big[\sum_{p\in p(c)} \big(r_{\underline{p}}^c l_{\underline{p}}^c \pi_{\underline{p}}^c n_{\underline{p}}^{c,r} + r_{\overline{p}}^c l_{\overline{p}}^c \pi_{\overline{p}}^c n_{\overline{p}}^{c,r}\big) - A_c P_a\Big]. \tag{2.19}$$

Switching the summation over cells and the summation over nodes at the right-hand side of Eq. (2.19), it can be rewritten as

$$\frac{\mathrm{d}}{\mathrm{d}t}\Big(\sum_c m_c u_c^r\Big) = -\sum_p \sum_{c\in c(p)} \big(r_{\underline{p}}^c l_{\underline{p}}^c \pi_{\underline{p}}^c n_{\underline{p}}^{c,r} + r_{\overline{p}}^c l_{\overline{p}}^c \pi_{\overline{p}}^c n_{\overline{p}}^{c,r}\big) + \sum_c A_c P_a. \tag{2.20}$$

Using the sufficient condition for total energy conservation (2.8), we have

$$\frac{\mathrm{d}}{\mathrm{d}t}\Big(\sum_c m_c u_c^r\Big) = \sum_c A_c P_a. \tag{2.21}$$

Eq. (2.21) refers to the conservation of the r-momentum, which, together with the conservation of the mass, z-momentum and total energy, guarantees the modified scheme (2.18) satisfies the Lax-Wendroff theorem.

Since the scheme (2.18) employs the same compatible discretization of the geometry conservation law (GCL) as that in the original scheme (2.15), it satisfies GCL naturally.

As to the entropy inequality, since we use the formulation of (2.16) to determine the pressure in the source term rather than P_c, we can not write a similar entropy inequality for the scheme (2.17) as that for the original scheme (2.13).

2.3.2 The issue of symmetry preservation

In this section, we will prove the modified scheme (2.18) can keep the spherical symmetry property computed on an equal-angle-zoned initial grid.

Theorem 2.1. *The modified scheme* (2.18) *can keep the one-dimensional spherical symmetry property computed on an equal-angle zoned initial grid. That is, if the solution has one-dimensional spherical symmetry at the initial time, then the computational solution will keep this symmetry with the time marching.*

Proof. Without loss of the generality, we only need to prove the solution of the modified scheme (2.18) can keep the spherical symmetry at the $(n+1)$th time step, if the solution is

known to be of spherical symmetry at the nth time step. Notice that, for the Lagrangian solution, symmetry preserving refers to the evolution of both the conserved variables and the grid.

1. Notations for the variables defined in the cell's local ξ-θ coordinates.

To facilitate the proof, we first simplify the vertex indices of the cell $\Omega(c)$ as $p=1,2,3,4$ (shown in Fig. 2) and rewrite the momentum equations in (2.17) along the cell's local ξ-θ coordinates. The rewritten semi-discrete scheme is of the following

$$m_c\frac{\mathrm{d}}{\mathrm{d}t}\Big(\frac{1}{\rho_c}\Big)=\sum_{p=1,4}(r^c_{\underline{p}}l^c_{\underline{p}}\mathbf{n}^c_{\underline{p}}+r^c_{\overline{p}}l^c_{\overline{p}}\mathbf{n}^c_{\overline{p}})\cdot\mathbf{u}_p, \tag{2.22a}$$

$$m_c\frac{\mathrm{d}}{\mathrm{d}t}u^\xi_c=-\sum_{p=1,4}\big(r^c_{\underline{p}}l^c_{\underline{p}}\pi^c_{\underline{p}}n^{c,\xi}_{\underline{p}}+r^c_{\overline{p}}l^c_{\overline{p}}\pi^c_{\overline{p}}n^{c,\xi}_{\overline{p}}\big)+A_cP_a\sin\theta_c, \tag{2.22b}$$

$$m_c\frac{\mathrm{d}}{\mathrm{d}t}u^\theta_c=-\sum_{p=1,4}\big(r^c_{\underline{p}}l^c_{\underline{p}}\pi^c_{\underline{p}}n^{c,\theta}_{\underline{p}}+r^c_{\overline{p}}l^c_{\overline{p}}\pi^c_{\overline{p}}n^{c,\theta}_{\overline{p}}\big)+A_cP_a\cos\theta_c, \tag{2.22c}$$

$$m_c\frac{\mathrm{d}}{\mathrm{d}t}E_c=-\sum_{p=1,4}\big(r^c_{\underline{p}}l^c_{\underline{p}}\pi^c_{\underline{p}}\mathbf{n}^c_{\underline{p}}+r^c_{\overline{p}}l^c_{\overline{p}}\pi^c_{\overline{p}}\mathbf{n}^c_{\overline{p}}\big)\cdot\mathbf{u}_p, \tag{2.22d}$$

where ξ is the radial direction passing through the cell center and the origin. For an equal-angle-zoned grid, the cell shown in Fig. 2 is an equal-sided trapezoid, it has the property that the angles between ξ and the two equal sides of the cell are the same. θ is the angular direction which is orthogonal to ξ, see Fig. 2. u^ξ_c and u^θ_c are the component values of velocity in the local ξ and θ directions respectively, $n^{c,\xi}_{\underline{p}}$,$n^{c,\xi}_{\overline{p}}$ and $n^{c,\theta}_{\underline{p}}$,$n^{c,\theta}_{\overline{p}}$ are the components of $\mathbf{n}^c_{\underline{p}}$ and $\mathbf{n}^c_{\overline{p}}$ along ξ and θ directions respectively. θ_c is set to be the angle between the local ξ direction and the z coordinate.

For the convenience of notation, we adopt the convention that variables without the superscript $n+1$ are those at the nth time step. Assume that at the nth time step the grid is a polar grid with equal angles (see Fig. 2) and the cell averages of the conserved variables including density, momentum and total energy are symmetrical on this grid, namely these variables in the cells with the same radial position are identical. Consider the cell Ω_c and its neighboring cells, in the local ξ-θ coordinates of the cell Ω_c, we have

$$\begin{cases}\rho_c=\rho_t=\rho_b=\rho_1, & \rho_l=\rho_0, & \rho_r=\rho_2,\\ P_c=P_t=P_b=P_1, & P_l=P_0, & P_r=P_2,\\ \xi_1=\xi_4=\xi_l, & \xi_2=\xi_3=\xi_r, & \\ \mathbf{u}_c=(u_1,0), & \mathbf{u}_l=(u_0,0), & \mathbf{u}_r=(u_2,0),\end{cases} \tag{2.23}$$

where $\{\xi_k,k=1,4\}$ are the distance of the four vertices of the cell Ω_c from the origin respectively, and $\{u_k,k=0,2\}$ are the magnitude of the cell velocity in the relevant cells.

Next we explain some notations concerning the grid geometry. For the cell Ω_c, the lengths of the cell edges are denoted as $\{l_{12},l_{23},l_{34},l_{41}\}$. Since the grid is symmetrical, we

can define them as

$$l_{12}=l_{34}=l_m, \qquad l_{14}=l_l, \qquad l_{23}=l_r. \tag{2.24}$$

For the convenience of proof, in the following, we will project all the variables relative to the determination of the cell's and nodal velocity to the cell's local ξ-θ coordinates. For example, the outward normal direction of the cell's four edges in the local ξ-θ coordinates are as follows

$$\mathbf{n}_{12}=(n_{12}^{\xi},n_{12}^{\theta})=\Big(-\sin\frac{\Delta\theta}{2},-\cos\frac{\Delta\theta}{2}\Big), \qquad \mathbf{n}_{23}=(n_{23}^{\xi},n_{23}^{\theta})=(1,0),$$
$$\mathbf{n}_{34}=(n_{34}^{\xi},n_{34}^{\theta})=\Big(-\sin\frac{\Delta\theta}{2},\cos\frac{\Delta\theta}{2}\Big), \qquad \mathbf{n}_{41}=(n_{41}^{\xi},n_{41}^{\theta})=(-1,0).$$

2. The proof of grid symmetry preservation.

In the case of a one-dimensional spherical flow computed on an equal angle polar grid, Maire in the paper [14] has already given the proof that the nodal velocity given by (2.9)-(2.11) is radial and independent of the angular cell position which means the symmetry preservation of the grid. From the results of the vertex velocity shown in [14], we can deduce that the velocities at each vertex for the cell Ω_c in its local ξ-θ coordinates are of the following form

$$u_1^{\xi}=u_4^{\xi}=\frac{z_0u_0+z_1u_1-(P_1-P_0)}{z_0+z_1}, \qquad u_1^{\theta}=-u_4^{\theta}=-\frac{z_0u_0+z_1u_1-(P_1-P_0)}{z_0+z_1}\tan\frac{\Delta\theta}{2}, \tag{2.25a}$$
$$u_2^{\xi}=u_3^{\xi}=\frac{z_1u_1+z_2u_2-(P_2-P_1)}{z_1+z_2}, \qquad u_2^{\theta}=-u_3^{\theta}=-\frac{z_1u_1+z_2u_2-(P_2-P_1)}{z_1+z_2}\tan\frac{\Delta\theta}{2}, \tag{2.25b}$$

where $z_0=\rho_0a_0$, $z_1=\rho_1a_1$ and $z_2=\rho_2a_2$. $\{a_0,a_1,a_2\}$ are the speeds of sound in the cells $\{\Omega_l,\Omega_c,\Omega_r\}$ respectively.

3. The proof of symmetry preservation for the conserved variables.

To specific, we need to prove the symmetry preservation of the evolved variables such as density, cell velocity and total energy.

We will first write each variable appearing at the right-hand side of (2.22) in details. By the following simple manipulation, the nodal pressures can be obtained

$$\pi_{\underline{1}}^{c}=P_1-z_1(\mathbf{u}_1-\mathbf{u}_c)\cdot\mathbf{n}_{41}=\frac{z_1P_0+z_0P_1-z_0z_1(u_1-u_0)}{z_0+z_1}, \tag{2.26a}$$
$$\pi_{\overline{1}}^{c}=P_1-z_1(\mathbf{u}_1-\mathbf{u}_c)\cdot\mathbf{n}_{12}=P_1-z_1u_1\sin\frac{\Delta\theta}{2}, \tag{2.26b}$$

where $\mathbf{u}_c=(u_1,0)$ and $\mathbf{u}_1=(u_1^{\xi},u_1^{\theta})$.

Similarly

$$\pi^c_{\underline{2}}=\pi^c_{\underline{3}}=\pi^c_{\underline{4}}=\pi^c_{\underline{1}}=P_1-z_1u_1\sin\frac{\Delta\theta}{2}, \tag{2.27a}$$

$$\pi^c_{\underline{4}}=\pi^c_{\underline{1}}=\frac{z_1P_0+z_0P_1-z_0z_1(u_1-u_0)}{z_0+z_1}, \tag{2.27b}$$

$$\pi^c_{\underline{2}}=\pi^c_{\underline{3}}=\frac{z_2P_1+z_1P_2-z_1z_2(u_2-u_1)}{z_1+z_2}. \tag{2.27c}$$

For the simplicity of description, we denote

$$P_m=P_1-z_1u_1\sin\frac{\Delta\theta}{2}, \qquad P_l=\frac{z_1P_0+z_0P_1-z_0z_1(u_1-u_0)}{z_0+z_1},$$
$$P_r=\frac{z_2P_1+z_1P_2-z_1z_2(u_2-u_1)}{z_1+z_2}, \qquad u_l=\frac{z_0u_0+z_1u_1-(P_1-P_0)}{z_0+z_1},$$
$$u_r=\frac{z_1u_1+z_2u_2-(P_2-P_1)}{z_1+z_2}.$$

By the formula (2.16), we have

$$P_a=P_m=P_1-z_1u_1\sin\frac{\Delta\theta}{2}. \tag{2.28}$$

The other corresponding variables appearing at the right hand side of (2.22) can be described in the following details

$$l^c_{\underline{1}}=l^c_{\underline{4}}=\frac{1}{2}l_l, \qquad l^c_{\underline{1}}=l^c_{\underline{2}}=l^c_{\underline{3}}=l^c_{\underline{4}}=\frac{1}{2}l_m, \qquad l^c_{\underline{2}}=l^c_{\underline{3}}=\frac{1}{2}l_r, \tag{2.29a}$$

$$\left(n^{c,\xi}_{\underline{1}},n^{c,\theta}_{\underline{1}}\right)=\left(n^{c,\xi}_{\underline{4}},n^{c,\theta}_{\underline{4}}\right)=\mathbf{n}_{41}=(-1,0), \tag{2.29b}$$

$$\left(n^{c,\xi}_{\underline{2}},n^{c,\theta}_{\underline{2}}\right)=\left(n^{c,\xi}_{\underline{1}},n^{c,\theta}_{\underline{1}}\right)=\mathbf{n}_{12}=\left(-\sin\frac{\Delta\theta}{2},-\cos\frac{\Delta\theta}{2}\right), \tag{2.29c}$$

$$\left(n^{c,\xi}_{\underline{3}},n^{c,\theta}_{\underline{3}}\right)=\left(n^{c,\xi}_{\underline{2}},n^{c,\theta}_{\underline{2}}\right)=\mathbf{n}_{23}=(1,0), \tag{2.29d}$$

$$\left(n^{c,\xi}_{\underline{4}},n^{c,\theta}_{\underline{4}}\right)=\left(n^{c,\xi}_{\underline{3}},n^{c,\theta}_{\underline{3}}\right)=\mathbf{n}_{34}=\left(-\sin\frac{\Delta\theta}{2},\cos\frac{\Delta\theta}{2}\right), \tag{2.29e}$$

$$r^c_{\underline{1}}+r^c_{\underline{2}}=(\xi_l+\xi_r)\sin\left(\theta_c-\frac{\Delta\theta}{2}\right), \qquad r^c_{\underline{3}}+r^c_{\underline{4}}=(\xi_l+\xi_r)\sin\left(\theta_c+\frac{\Delta\theta}{2}\right), \tag{2.29f}$$

$$r^c_{\underline{2}}+r^c_{\underline{3}}=2\sin\theta_c\cos\frac{\Delta\theta}{2}\xi_r, \qquad r^c_{\underline{1}}+r^c_{\underline{4}}=2\sin\theta_c\cos\frac{\Delta\theta}{2}\xi_l. \tag{2.29g}$$

Substituting (2.26)-(2.29) into (2.22), we get

$$m_c\frac{\mathrm{d}}{\mathrm{d}t}\begin{pmatrix}\rho_c^{-1}\\ u_c^{\xi}\\ u_c^{\theta}\\ E_c\end{pmatrix}=\begin{pmatrix}\sin\theta_c\cos\frac{\Delta\theta}{2}(\xi_rl_ru_r-\xi_ll_lu_l)\\ \sin\theta_c\left[\frac{1}{2}(\xi_l+\xi_r)l_mP_m\sin\Delta\theta+\xi_ll_lP_l-\xi_rl_rP_r\right]+A_cP_m\sin\theta_c\\ -\frac{1}{2}(\xi_l+\xi_r)l_mP_m\sin\Delta\theta\cos\theta_c+A_cP_m\cos\theta_c\\ -\sin\theta_c\cos\frac{\Delta\theta}{2}(\xi_rl_ru_rP_r-\xi_ll_lu_lP_l)\end{pmatrix}$$

$$= \begin{pmatrix} \sin\theta_c \cos\frac{\Delta\theta}{2}(\xi_r l_r u_r - \xi_l l_l u_l) \\ \sin\theta_c(-\xi_r l_r P_r + \xi_l l_l P_l + 2A_c P_m) \\ -A_c P_m \cos\theta_c + A_c P_m \cos\theta_c \\ -\sin\theta_c \cos\frac{\Delta\theta}{2}(\xi_r l_r u_r P_r - \xi_l l_l u_l P_l) \end{pmatrix} = \sin\theta_c \begin{pmatrix} \cos\frac{\Delta\theta}{2}(\xi_r l_r u_r - \xi_l l_l u_l) \\ -(\xi_r l_r P_r - \xi_l l_l P_l) + 2A_c P_m \\ 0 \\ -\cos\frac{\Delta\theta}{2}(\xi_r l_r u_r P_r - \xi_l l_l u_l P_l) \end{pmatrix}. \tag{2.30}$$

Since the cell is an equal-sided trapezoid, we have

$$m_c = \rho_1 V_c = \rho_1 r_c A_c = \rho_1 \xi_c A_c \sin\theta_c, \tag{2.31}$$

where r_c and ξ_c are the values of r and ξ at the cell center respectively.

Thus from (2.30) and (2.31), we have

$$\frac{\mathrm{d}}{\mathrm{d}t} \begin{pmatrix} \rho_c^{-1} \\ u_c^{\xi} \\ u_c^{\theta} \\ E_c \end{pmatrix} = \frac{1}{\rho_1 \xi_c A_c} \begin{pmatrix} \cos\frac{\Delta\theta}{2}(\xi_r l_r u_r - \xi_l l_l u_l) \\ -(\xi_r l_r P_r - \xi_l l_l P_l) + 2A_c P_m \\ 0 \\ -\cos\frac{\Delta\theta}{2}(\xi_r l_r u_r P_r - \xi_l l_l u_l P_l) \end{pmatrix}. \tag{2.32}$$

Finally we obtain the modified scheme (2.18) in the following detailed expression

$$\begin{pmatrix} (\rho_c^{n+1})^{-1} \\ u_c^{\xi,n+1} \\ u_c^{\theta,n+1} \\ E_c^{n+1} \end{pmatrix} = \begin{pmatrix} \rho_c^{-1} \\ u_c^{\xi} \\ u_c^{\theta} \\ E_c \end{pmatrix} + \frac{\Delta t}{\rho_1 \xi_c A_c} \begin{pmatrix} \cos\frac{\Delta\theta}{2}(\xi_r l_r u_r - \xi_l l_l u_l) \\ -(\xi_r l_r P_r - \xi_l l_l P_l) + 2A_c P_m \\ 0 \\ -\cos\frac{\Delta\theta}{2}(\xi_r l_r u_r P_r - \xi_l l_l u_l P_l) \end{pmatrix}. \tag{2.33}$$

From the formula (2.33), we can see the cell velocity is radial and the magnitude of all the conserved variables is independent of the angular position of the cell at the $(n+1)$th time step. The proof of the symmetry preservation property is thus completed.

So, the theorem is proved. □

3 Numerical results in the two-dimensional cylindrical coordinates

In this section, we perform numerical experiments in two-dimensional cylindrical coordinates. Purely Lagrangian computation, the ideal gas with $\gamma = 5/3$, the initially equal-angle polar grid and the modified scheme (2.18) are used in the following tests unless otherwise stated. Reflective boundary conditions are applied to the z and r axes in all the tests. For the velocity of vertices located at the z coordinate, we obtain it by imposing the boundary condition of zero normal velocity into the solver (2.9).

3.1 Accuracy test

We test the accuracy of the modified scheme (2.18) on a free expansion problem given in [21]. The initial computational domain is $[0,1]\times[0,\pi/2]$ defined in the polar coordinates. The gas is initially at rest with uniform density $\rho=1$ and pressure has the following distribution,

$$p=1-(z^2+r^2).$$

The analytical solution of the problem is as follows,

$$R(t)=\sqrt{1+2t^2}, \qquad u_{\tilde{\xi}}(z,r,t)=\frac{2t}{1+2t^2}\sqrt{z^2+r^2},$$
$$\rho(z,r,t)=\frac{1}{R^3}, \qquad p(z,r,t)=\frac{1}{R^5}\Big(1-\frac{z^2+r^2}{R^2}\Big),$$

where R is the radius of the free outer boundary and $u_{\tilde{\xi}}$ represents the value of velocity in the radial direction.

We perform the test both on an initially equal-angle polar grid and a random polar grid, see Fig. 3. For the random polar grid, each internal grid point is obtained by an independent random perturbation on the angular direction from a equal-angle polar grid which can be expressed as follows

$$\theta_{k,l}=\begin{cases}(l-1)\Delta\theta, & k=1,K \text{ or } l=1,L,\\ (l-1)\Delta\theta+c_1c_{k,l}\Delta\theta, & \text{else},\end{cases}$$
$$z_{k,l}=\frac{k-1}{K-1}\cos\theta_{k,l}, \quad r_{k,l}=\frac{k-1}{K-1}\sin\theta_{k,l}, \quad 1\le k\le K, \quad 1\le l\le L,$$

where $(z_{k,l},r_{k,l})$ is the z-r coordinate of the grid points with the sequential indices (k,l), $k=1,\cdots,K$, $l=1,\cdots,L$ in the radial and angular directions respectively. K,L represent the

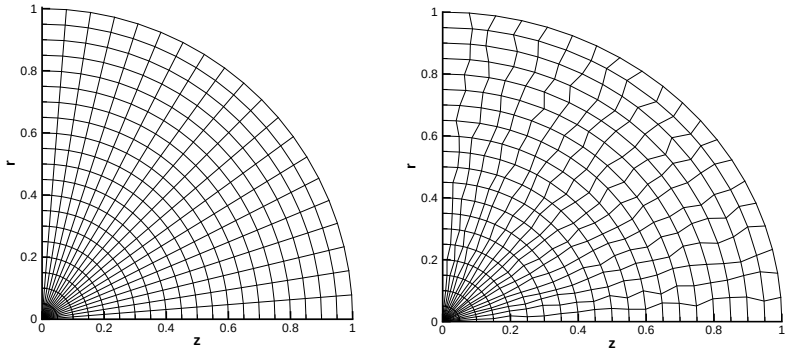

Figure 3: The initial grid of the free expansion problem with 20×20 cells. Left: equal-angle polar grid; Right: random polar grid.

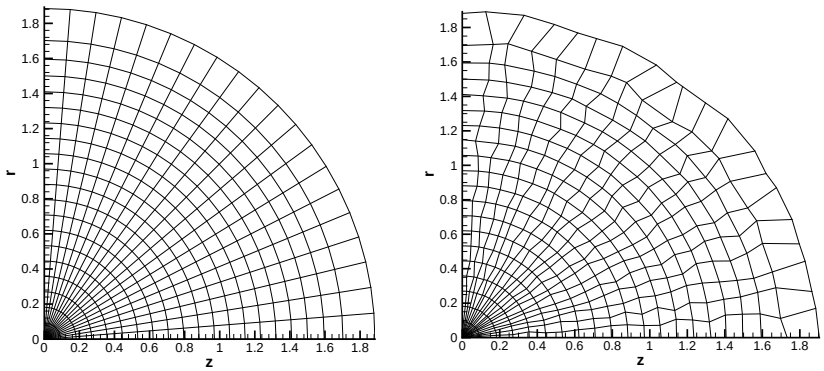

Figure 4: The grid of the free expansion problem with 20×20 cells at $t=1$. Left: equal-angle polar grid; Right: random polar grid.

number of grid points in the above mentioned two directions. $\Delta\theta=\pi/2(L-1)$. $-0.5\leq c_{k,l}\leq 0.5$ is the random number, c_1 is a parameter which is chosen as 0.5 in this test.

Free boundary condition is applied on the outer boundary. Fig. 4 shows the final grid. We can clearly observe symmetry in the left figure. The errors of the scheme on

Table 1: Errors of the scheme in 2D cylindrical coordinates for the free expansion problem using $K\times L$ initially equal-angle polar grid cells.

$K=L$	Norm	Density	order	Momentum	order	Energy	order
20	L_1	0.97E-2		0.13E-1		0.64E-2	
	L_∞	0.16E-1		0.19E-1		0.11E-1	
40	L_1	0.53E-2	0.88	0.67E-2	0.91	0.34E-2	0.90
	L_∞	0.77E-2	1.03	0.11E-1	0.83	0.52E-2	1.03
80	L_1	0.28E-2	0.91	0.35E-2	0.95	0.18E-2	0.94
	L_∞	0.36E-2	1.07	0.58E-2	0.90	0.28E-2	0.89
160	L_1	0.15E-2	0.93	0.18E-2	0.97	0.92E-3	0.96
	L_∞	0.19E-2	0.93	0.30E-2	0.94	0.15E-2	0.93

Table 2: Errors of the scheme in 2D cylindrical coordinates for the free expansion problem using $K\times L$ initially random polar grid cells.

$K=L$	Norm	Density	order	Momentum	order	Energy	order
20	L_1	0.94E-2		0.12E-1		0.62E-2	
	L_∞	0.16E-1		0.19E-1		0.11E-1	
40	L_1	0.50E-2	0.91	0.65E-2	0.93	0.33E-2	0.92
	L_∞	0.84E-2	0.89	0.12E-1	0.75	0.67E-2	0.69
80	L_1	0.27E-2	0.89	0.34E-2	0.95	0.17E-2	0.93
	L_∞	0.47E-2	0.86	0.62E-2	0.89	0.35E-2	0.91
160	L_1	0.14E-2	0.92	0.17E-2	0.97	0.88E-3	0.95
	L_∞	0.25E-2	0.89	0.35E-2	0.84	0.19E-2	0.92

these two kinds of grid at $t=1$ are listed in Tables 1-2 which are measured on the interval $[K/5,4K/5]\times[1,L]$ to remove the influence from the boundary. From both of the tables, we can see the expected first order accuracy for all the evolved conserved variables.

3.2 Non-oscillatory tests

Example 3.1. (The Noh problem in a cylindrical coordinate system on the polar grid [19]).

We test the Noh problem which is a well known test problem widely used to validate Lagrangian scheme in the regime of strong shock waves. In this test case, a cold gas with unit density and zero internal energy is given with an initial inward radial velocity of magnitude 1. The equal-angle polar grid is applied in the 1/4-circle computational domain defined in the polar coordinates by $[0,1]\times[0,\pi/2]$. The shock is generated in a perfect gas by bringing the cold gas to rest at the origin. The analytical post shock density is 64 and the shock speed is 1/3. The comparison of the final grid with 20×20 cells

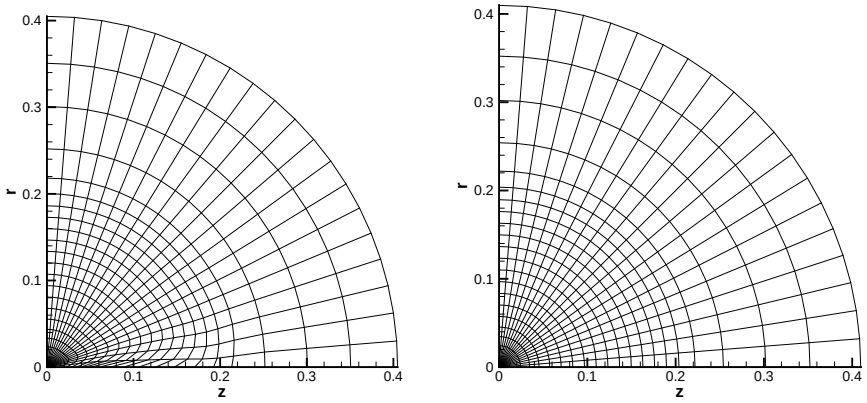

Figure 5: The results of the Noh problem with 20×20 cells at $t=0.6$. Left: the original scheme (2.15); Right: the modified scheme (2.18).

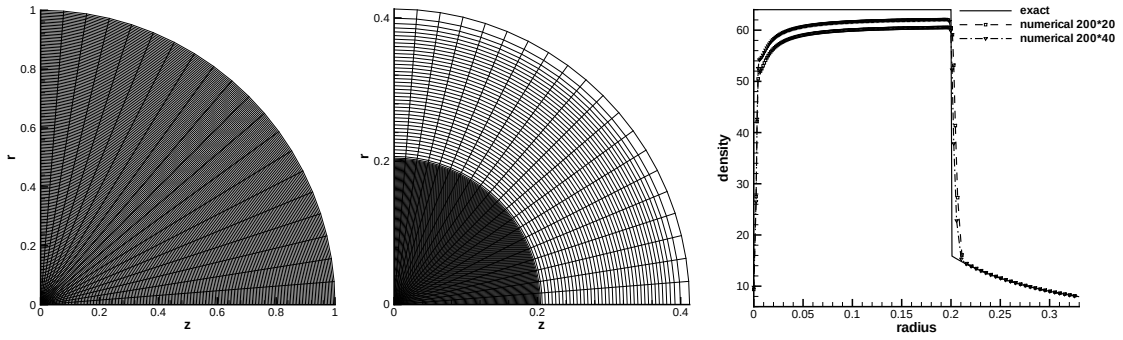

Figure 6: The results of the Noh problem at $t=0.6$. Left: initial grid with 200×20 cells; Middle: final grid with 200×20 cells; Right: density vs radial radius with 200×20 and 200×40 cells respectively. Solid line: exact solution; dashed line: computational solution.

between the original scheme (2.15) and the modified scheme (2.18) is given in Fig. 5 which demonstrates the improvement of the symmetry property for the modified scheme. Fig. 6 shows the results of the modified scheme including the final grid with 200×20 cells and density as a function of radial radius for two different angular zonings (200×20, 200×40) at $t=0.6$. From Fig. 6, we observe the results are symmetrical and non-oscillatory. The shock location and the shock magnitude are closer to those of the analytical solution with the grid refinement in the angular direction, which reflects the convergence trend of the numerical solution toward the analytical solution.

Example 3.2. (The spherical Sedov problem in a cylindrical coordinate system on the polar grid [21]).

We perform our test on the spherical Sedov blast wave problem in a cylindrical coordinate system as an example of a diverging shock wave. The initial computational domain is a 1/4-circle region defined in the polar coordinates by $[0,1.125]\times[0,\pi/2]$. The initial condition consists of unit density, zero velocity and zero specific internal energy except in the cells connected to the origin where they share a total value of 0.2468. Reflective boundary condition is applied on the outer boundary. The analytical solution is a shock at radius unity at time unity with a peak density of 4. Fig. 7 shows the comparison of the final grid with 20×20 cells between the original scheme (2.15) and the modified scheme (2.18). We can see that the latter has a perfect symmetry property. The final grid, density as a function of the radial radius and surface of density with 100×30 cells obtained by the modified scheme are displayed in Fig. 8. We also observe the expected symmetry in the plot of grid. The shock position and peak density coincide with those of the analytical solution very well and there is no spurious oscillation, demonstrating the good performance of the scheme in symmetry preserving, non-oscillation and accuracy properties.

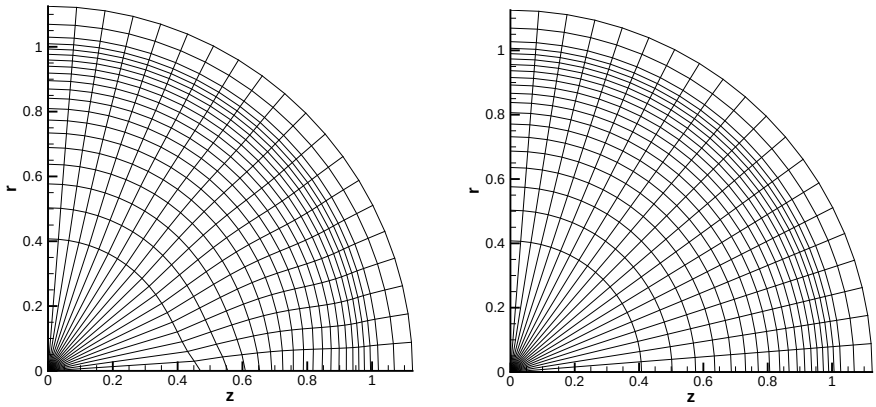

Figure 7: The results of the Sedov problem with 20×20 cells at $t=1.0$. Left: the original scheme (2.15); Right: the modified scheme (2.18).

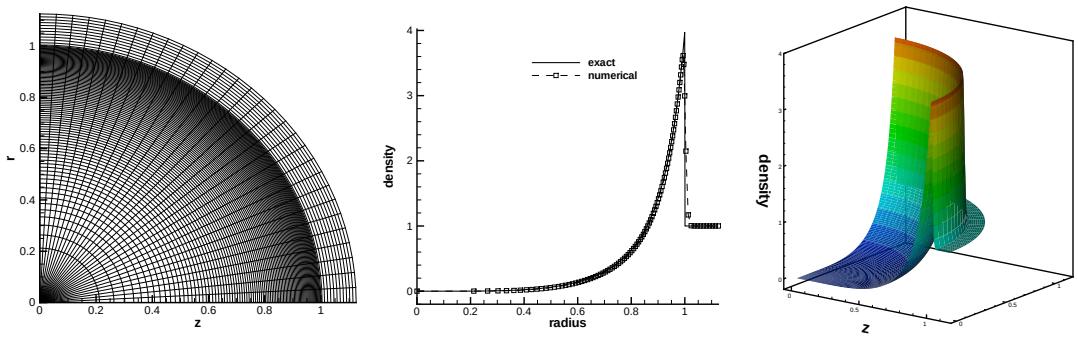

Figure 8: The result of the Sedov problem with 100×30 cells at $t=1.0$. Left: final grid; Middle: density vs radial radius. Solid line: exact solution; dashed line: computational solution; Right: surface of density.

Example 3.3. (The one-dimensional spherical Sod Riemann problem).

The modified scheme (2.18) is tested on the Sod Riemann problem in the cylindrical coordinates. The initial computational domain is a 1/4-circle region defined in the polar coordinates by $[0,20]\times[0,\pi/2]$. Its initial condition is as follows

$$(\rho,u_\xi,p)=(1.0,0,1.0),\ \ 0\le\xi\le10,\qquad (\rho,u_\xi,p)=(0.125,0,0.1),\ \ 10<\xi\le20.$$

Reflective boundary condition is applied on the outer boundary. The reference solution is the converged result obtained by using a one-dimensional second-order Eulerian code in the spherical coordinate with 10000 grid points. Fig. 9 shows the numerical results of the grid and density as a function of the radial radius and the surface of density performed by the modified scheme with 400×10 equal-angle polar cells at $t=1.4$. We observe the good behavior of the scheme in symmetry and the good agreement between the numerical result and the reference solution.

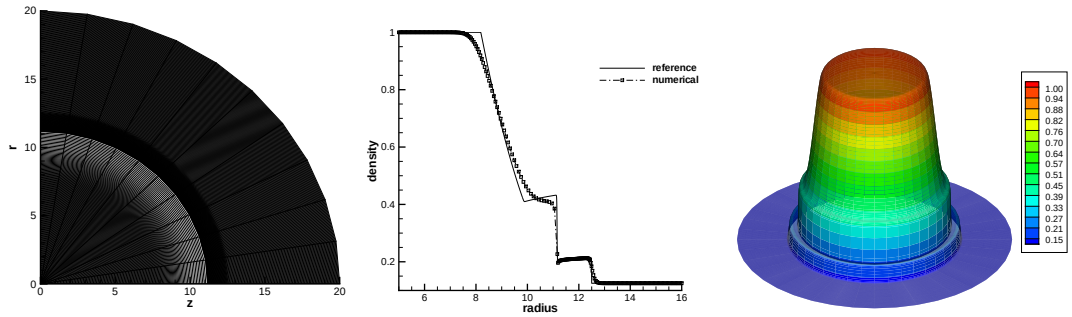

Figure 9: The results of the Sod problem at $t=1.4$. Left: final grid with 400×10 cells; Middle: density versus radial radius. Solid line: exact solution; dashed line: computational solution; Right: surface of density in the whole circle region obtained by a mirror image.

Example 3.4. (Kidder's isentropic compression problem [11,14]).

This problem is a self-similar isentropic problem which is usually used to validate the capability of a Lagrangian scheme in simulating a spherical isentropic compression. At

the initial time, the shell with a ring shape constitutes the computational region $[\xi_1,\xi_2]\times[0,\pi/2]$ in the polar coordinates, where $\xi_1=0.9$ is the internal radius and $\xi_2=1$ is the external radius. The initial density and pressure ρ_0,P_0 are expressed as follows

$$\rho_0(\xi)=\Big(\frac{\xi_2^2-\xi^2}{\xi_2^2-\xi_1^2}\rho_1^{\gamma-1}+\frac{\xi^2-\xi_1^2}{\xi_2^2-\xi_1^2}\rho_2^{\gamma-1}\Big)^{\frac{1}{\gamma-1}},\qquad P_0(\xi)=s(\rho_0(\xi))^\gamma,$$

where $\rho_1=6.31\times10^{-4}$, $\rho_2=10^{-2}$, $s=2.15\times10^4$, $\gamma=5/3$. The pressure $P_1(t)$ and $P_2(t)$ are imposed continuously at the internal and external boundary respectively which have the following representation

$$P_1(t)=P_1^0a(t)^{-\frac{2\gamma}{\gamma-1}},\qquad P_2(t)=P_2^0a(t)^{-\frac{2\gamma}{\gamma-1}},$$

where $P_1^0=0.1$, $P_2^0=10$ and $a(t)=\sqrt{1-(t/\tau)^2}$ in which $\tau=6.72\times10^{-3}$ is the focusing time of the shell and $t\in[0,\tau)$ is the evolving time.

Denoting $\zeta(\xi,t)$ to be the radius at time t of a point initially located at radius ξ, its analytical solution is $\zeta(\xi,t)=a(t)\xi$. The analytical solutions of three fundamental variables for this problem in spherical geometry are as follows

$$\rho(\zeta(\xi,t),t)=\rho_0(\xi)a(t)^{-\frac{2}{\gamma-1}},\quad u(\zeta(\xi,t),t)=\xi\frac{\mathrm{d}}{\mathrm{d}t}a(t),\quad p(\zeta(\xi,t),t)=P_0(\xi)a(t)^{-\frac{2\gamma}{\gamma-1}}.$$

We test the modified scheme (2.18) on the problem with 80×40, 160×80, 320×160 cells respectively. The final time is set to be $t=0.99\tau$. Fig. 10 shows the initial and final grids and the time evolution of the position of the external boundary with 40×20 grids. Fig. 11 shows the results of density, velocity and pressure at the final time. From these figures, we can see the perfect symmetry in the grid. The trajectory of the external boundary coincides with the analytical solution quite well. The numerical solutions of density, velocity and pressure converge to the analytical solutions asymptotically.

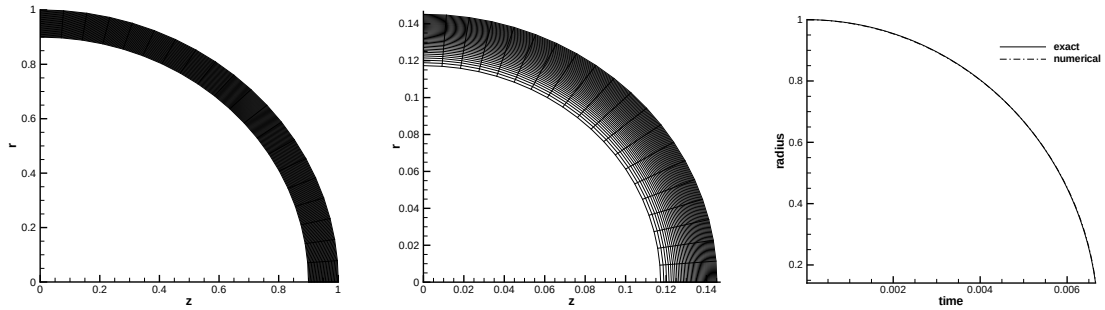

Figure 10: The results of the Kidder problem with 40×20 grids. Left: initial grid; Middle: final grid at $t=0.99\tau$; Right: trajectory of external boundary compared with the exact solution. Solid line: exact solution; dashed line: computational solution.

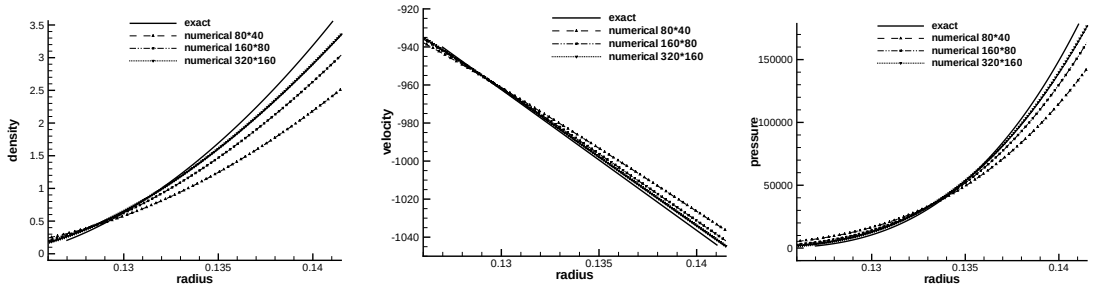

Figure 11: The results of the Kidder problem at $t=0.99\tau$ with three different zonings. Left: density vs radial radius; Middle: velocity vs radial radius; Right: pressure vs radial radius. Solid line: exact solution; dashed line: computational solution.

Example 3.5. (Implosion problem of Lazarus [12]).

The implosion problem of Lazarus is a self-similar problem. At the initial time, a sphere of unit radius with unit density and zero specific internal energy is driven by the following inward radial velocity

$$u_{\xi}(t)=\frac{-\alpha f}{(1-ft)^{1-\alpha}}, \tag{3.1}$$

where $\alpha=0.6883545$, $f=1-\varepsilon t-\delta t^3$, $\varepsilon=0.185$, $\delta=0.28$.

We test the problem on a grid of 200×30 cells in the initial computational domain $[0,1]\times[0,\pi/2]$ defined in the polar coordinates. The numerically converged result computed using a one-dimensional second-order Lagrangian code in the spherical coordinate with 10000 cells is used as a reference solution. We display the results of the modified scheme (2.18) using 200×30 and 200×60 cells in Fig. 12. In the plot of grid, we notice the expected symmetry. In the plot of density, we observe the non-oscillatory and accurate numerical solution and the convergence tendency of the numerical results toward the reference solution.

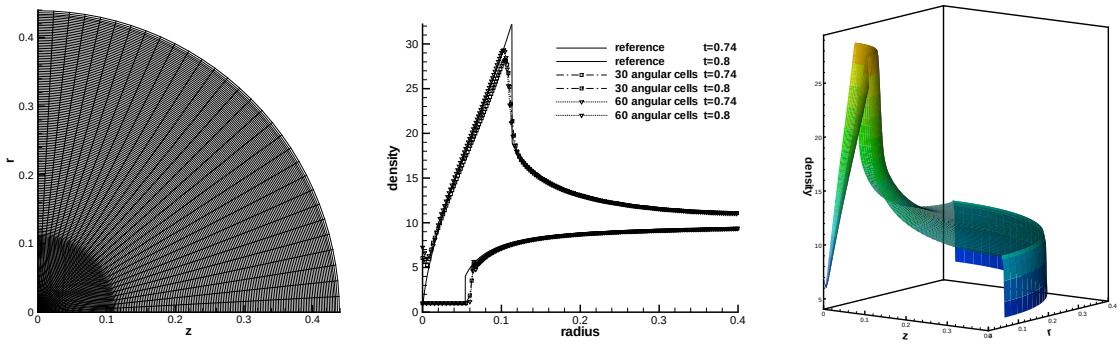

Figure 12: The results of the Lazarus problem. Left: final grid with 200×30 cells at $t=0.8$; Middle: density vs radial radius at $t=0.74$, 0.8 with 200×30 and 200×60 cells respectively. Solid line: reference solution; dashed line: computational solution; Right: surface of density at $t=0.8$ with 200×30 cells.

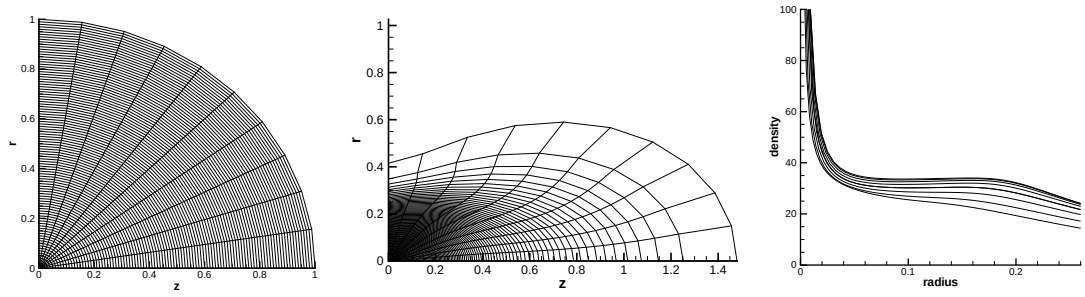

Figure 13: The results of the Coggeshall problem at $t=0.8$. Left: initial grid; Middle: final grid; Right: density versus the radial radius.

Example 3.6. (Coggeshall expansion problem [9]).

This is a two-dimensional adiabatic compression problem proposed by Coggeshall. We attempt to apply it to test the performance of the modified scheme (2.18) on a truly two-dimensional problem. The computational domain consists of a quarter of a sphere of unit radius zoned with 100×10 cells. The initial density is unity and the initial velocity at the grid vertices is given as $(u_z,u_r)=(-z/4,-r)$. The specific internal energy of a cell is given as $e=(3z_c/8)^2$, where z_c is the z coordinate of the cell center. Fig. 13 shows the results of the grid and density plotted as a function of the radial radius along each radial line at the time of 0.8 when the analytical density is expected to be flat with a value of 37.4. From the figures, we can observe the numerical result agrees with the analytical solution except for the small region near the origin.

Example 3.7. (Spherical Sedov problem on the Cartesian grid).

We test the spherical Sedov blast wave in a cylindrical coordinate system on the initially rectangular grid. The initial computational domain is a 1.125×1.125 square consisting of 30×30 uniform cells. The initial density is unity and the initial velocity is zero. The specific internal energy is zero except in the cell connected to the origin where it has a value of 0.2468. Fig. 14 shows the results of the original scheme (2.15) and the modified scheme (2.18). From the figures, we can observe the results from the modified scheme are more satisfactory and more symmetrical even on the non-polar grid.

Example 3.8. (Spherical Noh problem on the Cartesian grid [19]).

At last, we test the spherical Noh problem on a Cartesian grid to verify the robustness of the scheme. This problem is a very severe test for a Lagrangian scheme computing on a Cartesian grid, since in this case the grid near the axes is easy to be distorted which has been addressed in [5]. The initial domain is $[0,1]\times[0,1]$. The initial state of the fluid is uniform with $(\rho,u_\xi,u_\theta,e)=(1,-1,0,10^{-5})$, where u_ξ,u_θ are the radial and angular velocities at the cell center. Reflective boundary conditions are applied on the left and lower boundaries. Free boundary condition is used on the right and upper boundary. The analytical solution is the same as that in Example 3.1. Fig. 15 shows the results of the original scheme (2.15) and the modified scheme (2.18) with 50×50 initially uniform rectangular

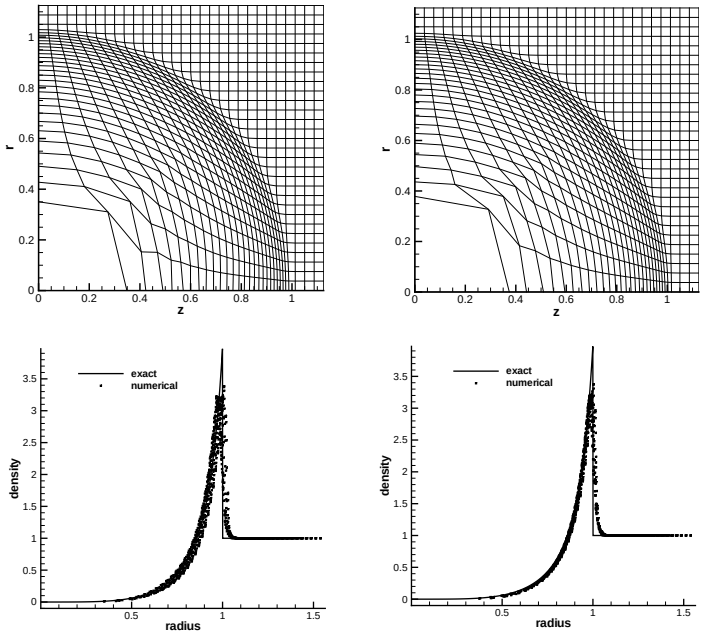

Figure 14: The results of the Sedov problem with 30×30 grids at $t=1.0$. Left: the original scheme (2.15); Right: the modified scheme (2.18). Top: final grid. Bottom: density vs radial radius.Solid line: exact solution; symbols: computational solution.

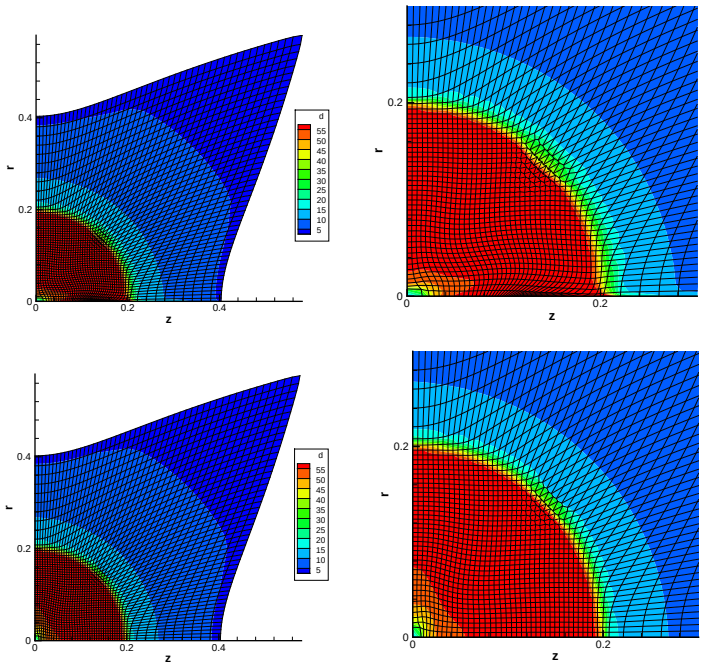

Figure 15: Grid and density contour for the Noh problem with 50×50 Cartesian cells at $t=0.6$. Top: the original scheme (2.15); Bottom: the modified scheme (2.18). Left: whole grid; Right: zoom on the region with shock.

cells at $t = 0.6$. From these figures, we can see that there is no grid distortion along the axes, the spherical symmetry is preserved better and the shock position is correct for the modified scheme, which demonstrate the robustness of the modified scheme in this problem on the Cartesian grid.

4 Concluding remarks

In this paper we apply the methodology proposed in our previous work [8] on Maire's first order control volume Lagrangian scheme [14]. The purpose of this work is to improve the scheme's property in symmetry preservation while maintaining its original good properties including geometric conservation law (GCL) and conservation of mass, momentum and total energy. The modified scheme is proven to have one-dimensional spherical symmetry in the two-dimensional cylindrical geometry for equal-angle-zoned initial grids. Several two-dimensional examples in the cylindrical coordinates have been presented which demonstrate the good performance of the modified scheme in symmetry, non-oscillation and robustness. The improvement of the modified scheme in accuracy constitutes our future work.

Acknowledgments

J. Cheng is supported in part by NSFC grants 10972043 and 10931004. Additional support is provided by the National Basic Research Program of China under grant 2011CB309702. C.-W. Shu is supported in part by ARO grant W911NF-08-1-0520 and NSF grant DMS-0809086.

References

[1] D. J. Benson, Momentum advection on a staggered mesh, J. Comput. Phys., 100 (1992), 143–162.
[2] D. J. Benson, Computational methods in Lagrangian and Eulerian hydrocodes, Comput. Methods Appl. Mech. Eng., 99 (1992), 235–394.
[3] E. J. Caramana, D. E. Burton, M. J. Shashkov and P. P. Whalen, The construction of compatible hydrodynamics algorithms utilizing conservation of total energy, J. Comput. Phys., 146 (1998), 227–262.
[4] E. J. Caramana, M. J. Shashkov and P. P. Whalen, Formulations of artificial viscosity for multidimensional shock wave computations, J. Comput. Phys., 144 (1998), 70–97.
[5] J. C. Campbell and M. J. Shashkov, A tensor artificial viscosity using a mimetic finite difference algorithm, J. Comput. Phys., 172 (2001), 739–765.
[6] J. Cheng and C.-W. Shu, A high order ENO conservative Lagrangian type scheme for the compressible Euler equations, J. Comput. Phys., 227 (2007), 1567–1596.
[7] J. Cheng and C.-W. Shu, A third order conservative Lagrangian type scheme on curvilinear meshes for the compressible Euler equation, Commun. Comput. Phys., 4 (2008), 1008–1024.

[8] J. Cheng and C.-W. Shu, A cell-centered Lagrangian scheme with the preservation of symmetry and conservation properties for compressible fluid flows in two-dimensional cylindrical geometry, J. Comput. Phys., 229 (2010), 7191–7206.
[9] S. V. Coggeshall and J. Meyer-ter-Vehn, Group invariant solutions and optimal systems for multidimensional hydrodynamics, J. Math. Phys., 33 (1992), 3585–3601.
[10] B. Després and C. Mazeran, Lagrangian gas dynamics in two dimensions and Lagrangian systems, Arch. Rational Mech. Anal., 178 (2005), 327–372.
[11] R. E. Kidder, Laser-driven compression of hollow shells: power requirements and stability limitations, Nuclear Fusion, 1 (1976), 3–14.
[12] R. Lazarus, Self-similar solutions for converging shocks and collapsing cavities, SIAM J. Numer. Anal., 18 (1981), 316–371.
[13] W. Liu, J. Cheng and C.-W. Shu, High order conservative Lagrangian schemes with Lax-Wendroff type time discretization for the compressible Euler equations, J. Comput. Phys., 228 (2009), 8872–8891.
[14] P.-H. Maire, A high-order cell-centered Lagrangian scheme for compressible fluid flows in two-dimensional cylindrical geometry, J. Comput. Phys., 228 (2009), 6882–6915.
[15] P.-H. Maire, R. Abgrall, J. Breil and J. Ovadia, A cell-centered Lagrangian scheme for compressible flow problems, SIAM J. Sci. Comput., 29 (2007), 1781–1824.
[16] L. G. Margolin and M. J. Shashkov, Using a curvilinear grid to construct symmetry-preserving discretizations for Lagrangian gas dynamics, J. Comput. Phys., 149 (1999), 389–417.
[17] C. D. Munz, On Godunov-type schemes for Lagrangian gas dynamics, SIAM J. Numer. Anal., 31 (1994), 17–42.
[18] J. von Neumann and R. D. Richtmyer, A method for the calculation of hydrodynamics shocks, J. Appl. Phys., 21 (1950), 232–237.
[19] W. F. Noh, Errors for calculations of strong shocks using an artificial viscosity and an artificial heat flux, J. Comput. Phys., 72 (1987), 78–120.
[20] W. D. Schulz, Two-dimensional Lagrangian hydrodynamic difference equations, Methods Comput. Phys., 3 (1964), 1–45.
[21] L. I. Sedov, Similarity and Dimensional Methods in Mechanics, Academic Press, New York, 1959.
[22] A. Solov'ev and M. Shashkov, Difference scheme for the Dirichlet particle method in cylindrical method in cylindrical coordinates, conserving symmetry of gas-dynamical flow, Differential Equations, 24 (1988), 817–823.
[23] M. L. Wilkins, Calculation of elastic plastic flow, Methods Comput. Phys., 3 (1964), 211–263.